IEICE TRANS. ELECTRON., VOL.E106–C, NO.10 OCTOBER 2023

PAPER

A New SIDGS-Based Tunable BPF Design Method with Controllable Bandwidth

Weiyu ZHOU[†a)] ***and*** **Koji WADA**[†b)]**,** ***Members***

SUMMARY This paper provides a new method to implement substrate integrated defected ground structure (SIDGS)-based bandpass filter (BPF) with adjustable frequency and controllable bandwidth. Compared with previous literature, this method implements a new SIDGS-like resonator capable of tunable frequency in the same plane as the slotted line using a varactor diode, increasing the design flexibility. In addition, the method solves the problem that the tunable BPF constituted by the SIDGS resonator cannot control the bandwidth by introducing a T-shaped non-resonant unit. The theoretical design method and the structural design are shown. Moreover, the configured structure is fabricated and measured to show the validity of the design method in this paper.

key words: *substrate integrated defected ground structure (SIDGS), tunable band-pass filter (BPF), controllable bandwidth*

1. Introduction

With the development of modern wireless systems, some current communication devices require miniaturization while also operating in multiple frequency bands. In order to satisfy the development needs of these communication devices, bandpass filters (BPFs) are constantly being updated and progressed. Therefore, there is a strong need for a BPF filter that can operate in multiple frequency bands while maintaining bandwidth and miniaturization.

SIDGS consists of slot lines and metal vias that surround the slots [1]. Compared with waveguides and SIWs [2], [3], it has a smaller volume [4], and also has a lower radiation loss [5]. Compared with a microstrip line [6], it has lower radiation loss, a more robust ability to resist interference from external circuits [7], and also has the characteristic of the compact structure of a microstrip line [8], [9]. Therefore, it can satisfy the requirements of miniaturization and low radiation loss at the same time. Regarding the realization of frequency adjustment, the more common method is to connect the resonator to a varactor diode [10]–[12] or MEMS to control the frequency [13], [14], or to adjust the length of slot lines manually [15]. It is also possible to use a particular substrate, such as liquid crystal materials [16], which a voltage can adjust the dielectric constant ratio of the substrate to achieve frequency tunability. The method of electronic control used in [10]–[14] cannot be directly applied to SIDGS for structural reasons. In [17], a harmonic-controlled SIDGS resonator is proposed, which uses a varactor diode to indirectly control the equivalent inductance of the SIDGS to change the resonant frequency. Additionally, there is a method to adjust the resonant frequency by crossing a varactor diode on both sides of the slot of CSRR and DGS (similar to SIDGS in structure), which changes the equivalent capacitance in the equivalent circuit [18]–[20]. In the above method, all the adjustment circuits must pass through the substrate, and there is a problem in that the center frequency and bandwidth cannot be controlled independently.

In this paper, a new center frequency adjustment method and bandwidth adjustment method are proposed, which enables the center frequency and bandwidth to be adjusted independently, and the control circuit of the center frequency will be in the same plane of the SIDGS and outside the SIDGS, significantly improving the flexibility of the design. The principles of frequency control and bandwidth control by this method are analyzed in detail in Sect. 2. In Sect. 3, the practical application of the frequency adjustment circuit and the bandwidth adjustment circuit is discussed, as well as the effect on the external Q value after loading a varactor diode on the port. Next, Sect. 4 presents the design of a tunable BPF with constant bandwidth. Finally, conclusions are given in Sect. 5.

2. Adjustment Methods of Center Frequency and Coupling Coefficient

2.1 An Adjustment Method of the Center Frequency

Figure 1 shows an SIDGS resonator cell designed for frequency adjustment. The cell consists of two parts, a C-shaped slotted line and metal vias surrounding the slot forming the SIDGS resonator part (the part inside the red dotted line), and a frequency adjustment circuit part consisting of an I-shaped slotted line loaded with capacitors and grounded metal vias.

When we change the capacitance of capacitor C, the scattering parameters shown in Fig. 2 can be obtained. By substituting the scattering parameters obtained in Fig. 2 into Eq. (1) [21], we can obtain the equivalent impedance at the resonant frequency under different capacitances of about 50Ω above 3.1GHz [22]. This is because, on the whole, Although the width of the slot line of SIDGS is the same, it is not a uniform transmission line, it does not have a constant

Manuscript received December 1, 2022.
Manuscript revised February 21, 2023.
Manuscript publicized March 28, 2023.

[†]The authors are with the Graduate School of Informatics and Engineering at the University of Electro-Communications, Chofushi, 182–8585 Japan.
a) E-mail: s2041008@edu.cc.uec.ac.jp
b) E-mail: wada.koji@uec.ac.jp

DOI: 10.1587/transele.2022ECP5062

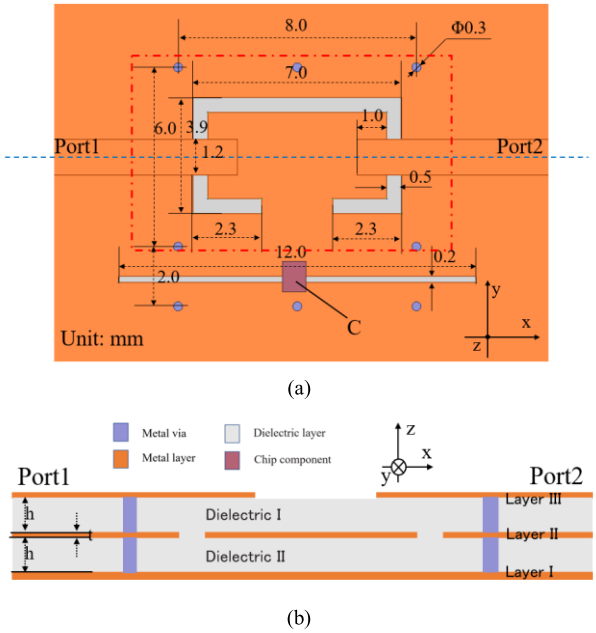

Fig. 1 The structure of tunable SIDGS resonator unit. (a) Top view. (b) Section view along the blue dotted line. ε_r = 3.4, h = 0.5 mm, t = 18μm. Note that Via is not visible in (b), here is to show its positional relationship with the.

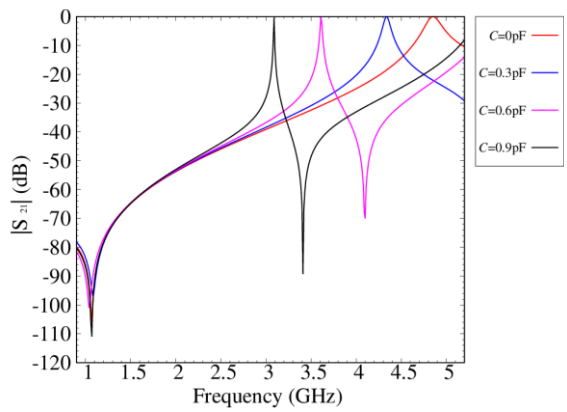

Fig. 2 Scattering parameters of SIDGS resonator unit at different C.

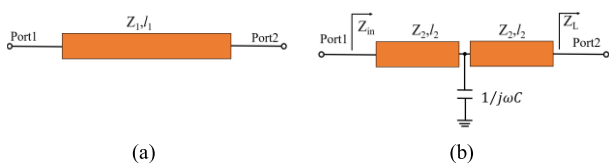

Fig. 3 (a) A transmission line with a characteristic impedance of 50Ω. (b) Equivalent circuit of SIDGS at resonant frequency.

characteristic impedance, but it can be regarded as a unit of periodic lumped elements. It is similar to complementary split rings resonators [23] in that the equivalent impedance keeps changing with frequency and resonates when it is equal to 50Ω. Therefore, its equivalent circuit is shown in Fig. 3, and it is equivalent to a transmission line with a characteristic impedance of 50Ω at the resonant frequency.

$$Z_B = \mp\frac{2b}{a-d\mp\sqrt{(a+d)^2-4}} \tag{1}$$

In Eq. (1), a, b, c, and d are ABCD parameters, which can be obtained from the simulation results. Where $a = \frac{(1+S_{11})(1-S_{22})+S_{12}S_{21}}{2S_{21}}$, $b = Z_0\frac{(1+S_{11})(1+S_{22})-S_{12}S_{21}}{2S_{21}}$, $c = \frac{1}{Z_0}\frac{(1-S_{11})(1-S_{22})-S_{12}S_{21}}{2S_{21}}$, $d = \frac{(1-S_{11})(1+S_{22})+S_{12}S_{21}}{2S_{21}}$, and the characteristic impedance of the source $Z_0 = 50\,\Omega$. S_{11}, S_{12}, S_{21}, and S_{22} are scattering parameters.

In Fig. 3, Z_1 and l_1 are the characteristic impedance and length of the 50Ω transmission line. Z_2 and l_2 are half of the characteristic impedance and length of SIDGS. Z_{in} (50Ω) and Z_L (50Ω) are input impedance and load impedance respectively.

According to Fig. 3, we can obtain Eq. (2) and Eq. (3).

$$[A] = \begin{bmatrix} \cos(\beta_1 l_1) & jZ_1\sin(\beta_1 l_1) \\ \frac{j\sin(\beta_1 l_1)}{Z_1} & \cos(\beta_1 l_1) \end{bmatrix} \tag{2}$$

$$\begin{aligned}[B] &= \begin{bmatrix} \cos(\beta_2 l_2) & jZ_1\sin(\beta_2 l_2) \\ \frac{j\sin(\beta_2 l_2)}{Z_2} & \cos(\beta_2 l_2) \end{bmatrix}\begin{bmatrix} 1 & 0 \\ j\omega_0 C & 1 \end{bmatrix}\begin{bmatrix} \cos(\beta_2 l_2) & jZ_1\sin(\beta_2 l_2) \\ \frac{j\sin(\beta_2 l_2)}{Z_2} & \cos(\beta_2 l_2) \end{bmatrix} \\ &= \begin{bmatrix} \cos(2\beta_2 l_2)-\frac{Z_2\omega_0 C}{2}\sin(2\beta_2 l_2) & jZ_2\sin(2\beta_2 l_2)-jZ_2^2\omega_0 sin^2(2\beta_2 l_2) \\ \frac{j\sin(2\beta_2 l_2)}{2Z_2}+j\omega_0 C cos^2(2\beta_2 l_2) & \cos(2\beta_2 l_2)-\frac{Z_2\omega_0 C}{2}\sin(2\beta_2 l_2) \end{bmatrix}\end{aligned} \tag{3}$$

β_x (x = 1 *or* 2) in Eq. (2) and Eq. (3) is the phase constant ω_0 is the central angular frequency.

At the resonant frequency f_0 (= $\omega_0/2\pi$), [A] = [B], and further, we can obtain Eq. (4). Since SIDGS is a half-wavelength resonator [24], we can obtain Eq. (5) by substituting $\beta_1 l_1 = \pi$ into Eq. (4).

$$\mathrm{Cos}(\beta_1 l_1) = cos(2\beta_2 l_2) - \frac{Z_2\omega_0 C}{2}sin(2\beta_2 l_2) \tag{4}$$

$$C = \frac{2(\cos(2\beta_2 l_2)+1)}{\omega_0 Z_2\sin(2\beta_2 l_2)} \tag{5}$$

In Eq. (5),

$$\beta_2 = \frac{2\pi f_0\sqrt{\varepsilon_{reff}}}{c_o} \tag{6}$$

In Eq. (6), $c_o = 3\times10^8 m/s$ is the speed of light in a vacuum. ε_{reff} = 2.97 is the effective dielectric constant of SIDGS in Fig. 1.

In addition, since the equivalent resistance of SIDGS is 50Ω at the resonance frequency, Eq. (7) [25] can be listed according to Fig. 3, thus obtaining Eq. (8).

$$Z_{in} = Z_2 + \frac{1}{j\omega_0 C} + \frac{1/\omega_0^2 C^2}{Z_2 + 1/j\omega_0 C + Z_L} \tag{7}$$

$$Z_2 = \sqrt{Z_{in}^2 - \frac{2}{j\omega_0 C}} \tag{8}$$

Substituting Eq. (5) into Eq. (8), the resonant frequency

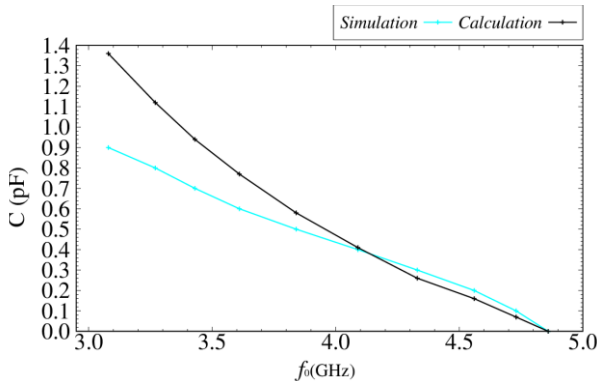

Fig. 4 Calculation and simulation results of C_f at different frequencies.

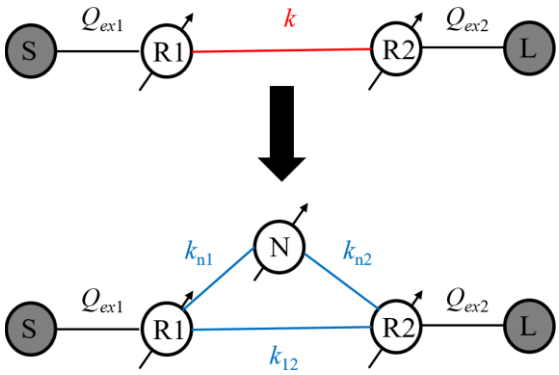

Fig. 5 Topology Logic for SIDGS Bandwidth Controllable.

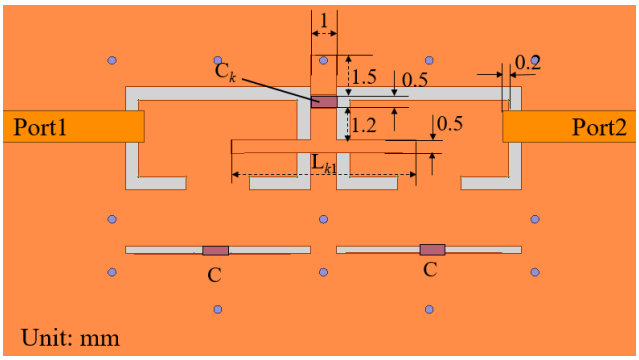

Fig. 6 Structure of the T-shaped non-resonator.

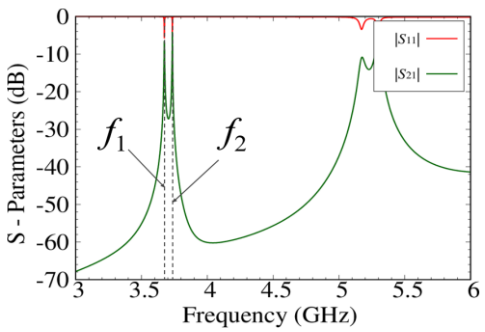

Fig. 7 An example of calculating coupling coefficient k.

under different capacitances can be obtained. The calculation results were obtained using Matlab R2020b. Taking the center frequency of 4.33GHz as an example, $Z_2 = 49.98 - j\,1.34\ \Omega$ and $C = 0.55 + j\,0.014$ pF are calculated. We will find that Z_2 in the calculation result is a complex value close to 50Ω, and C will also have a small imaginary part, which is considered the equivalent impedance generated by the I-shaped slot and the metal via. The final calculation result takes real part.

Comparing the calculated results with the model simulation results of HFSS 12.0, as shown in Fig. 4, we can find that the error is within 0.04 pF in the range of 4.09–4.86 GHz. However, the error generated becomes larger as the frequency decreases below 4.09 GHz. The error is considered to be the neglect of the influence from the I-slot when calculating the value of C. According to the above results, the resonant frequency can be predicted by the method in a certain range, the above equivalent circuit is reasonable, and the loading capacitance in the same plane of the SIDGS is also proved feasible.

2.2 An Adjustment Method of the Coupling Coefficient

Achieving independent control of the coupling between two SIDGS is an unsolved problem. SIDGS cannot be controlled by connecting two resonators with varactor diodes, similar to literatures [26], [27] because of the structural reasons. In this paper, a T-type non-resonator is provided between two SIDGS. By loading the varactor diode on the T-type non-resonator, the independent control of the coupling between the SIDGS can be achieved, as shown in Fig. 5.

According to Fig. 5, due to the addition of this structure, a coupling path (R1-k_{n1}-N-k_{n2}-R2) through the non-resonator is added to the original coupling of the two SIDGS resonators. The coupling between the SIDGS and the non-resonator can be changed by changing the bias voltage on the varactor on the non-resonator so that the total coupling k between the two SIDGS can be changed.

In order to study the influence of the structure of the T-type non-resonator on the coupling, the T-type non-resonator with different L_{k1} and different capacitances was simulated and calculated. The structure of T-type non-resonator is shown in Fig. 6. Figure 7 shows the simulation results when $L_{k1} = 7$ mm and $C_k = 1$ pF.

When calculating k, Eq. (9) is used [28].

$$k = \frac{f_2^2 - f_1^2}{f_2^2 + f_1^2} \tag{9}$$

In Eq. (9), f_1 and f_2 are the lower resonant frequency and the higher resonant frequency of the two resonators coupled, respectively, as shown in Fig. 7. The results obtained from Eq. (9) are collated in Fig. 8 and Fig. 9. According to Fig. 8, we found that the longer the length of L_{k1}, the greater the variation of k when adjusting C_k, and the greater the tuning range. In the extreme case when the length of L_{k1} is 0 mm, adjusting C_k does not cause k to change. We do not

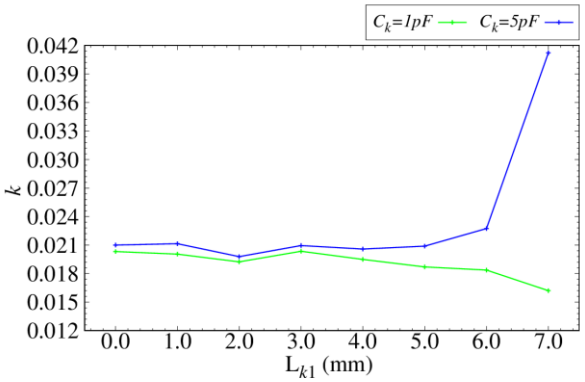

Fig. 8 When L_{k1} is changed, the change tendency of k.

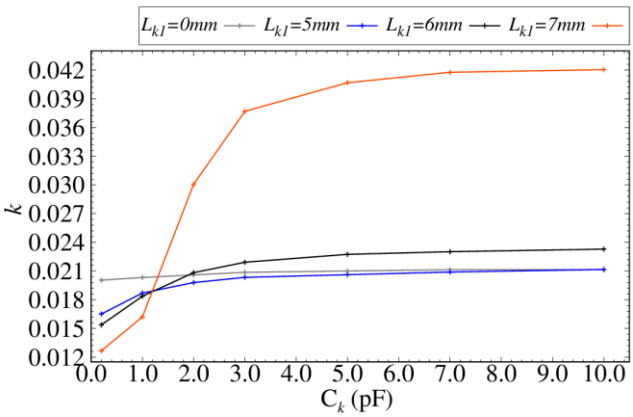

Fig. 9 When C_k is changed, the change tendency of k.

find any pattern in Fig. 8, but when we fix the length of L_{k1} as in Fig. 9, we can see that k increases and converges to a certain value as C_k increases. And the longer the length of L_{k1}, the more significant the change.

3. Design of a Tunable BPF

3.1 Calculation of Q_{ex} and k

To further verify the feasibility of the above method, a BPF with a frequency adjustment range of 3.7–4.2 GHz is designed, and a tunable BPF with a constant bandwidth of 100 MHz can be made by voltage control. The design specification of the tunable BPF is shown in Table 1. Since Q_{ex} and k change monotonically and continuously, and take the maximum and minimum values at 3.7 GHz and 4.2 GHz, only the results at 3.7 GHz and 4.2 GHz are calculated for Ref. [29].

3.2 Design of Frequency Adjustment Circuit

The reasonableness and validity of the method are verified in Sect. 2.1, but the circuit can not be directly used for the actual design of tunable BPF. A varactor diode needs to be used in the actual design, and a bias voltage needs to be applied. Therefore, it is also necessary to modify the structure of the frequency adjustment circuit of the SIDGS. The modified circuit is shown in Fig. 10.

Different C_f cases are simulated, and the relationship between C_f and f_0 is shown in Fig. 11. At 0.23–2.1 pF, f_0

Table 1 The design specifications

f_0(GHz)	Characteristics	Order	BW(MHz)	RL(dB)	Q_{ex}	k
3.7	Chebyshev	2	100(0.05dB)	19.4	52.2	0.0191
4.2	Chebyshev	2	100(0.05dB)	19.4	59.3	0.0169

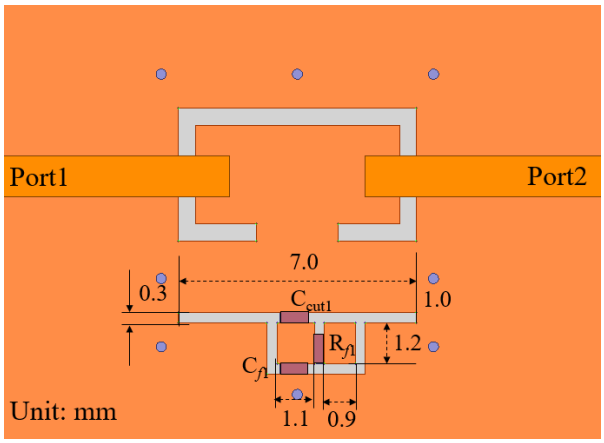

Fig. 10 Actual structure of the SIDGS resonator unit.

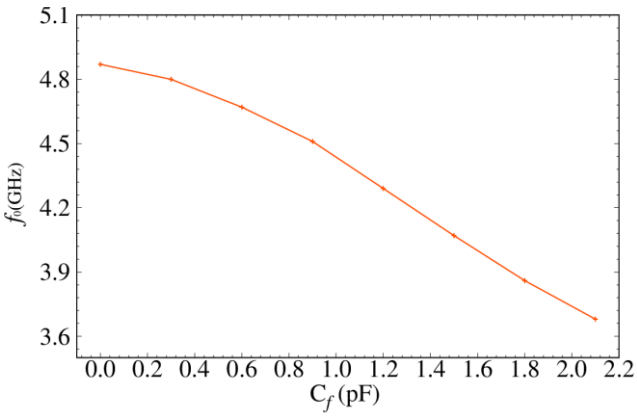

Fig. 11 When C_f is changed, the change tendency of f_0.

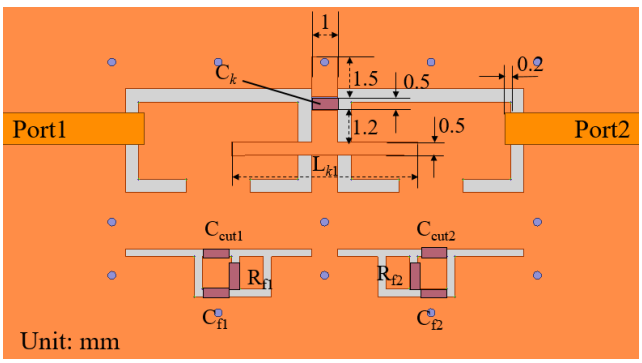

Fig. 12 Actual structure of the SIDGS loaded with T-type non-resonator.

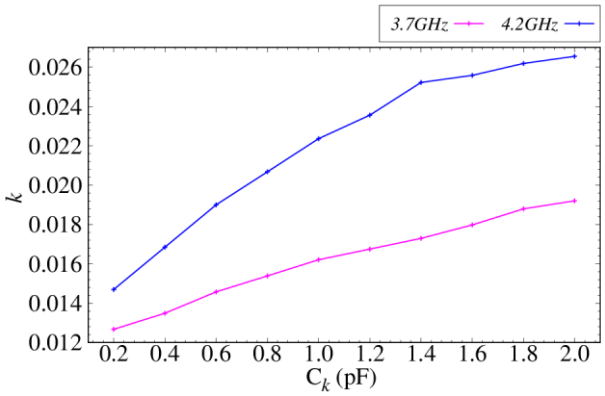

Fig. 13 At 3.7 GHz and 4.2 GHz, when changing C_k, the change tendency of k.

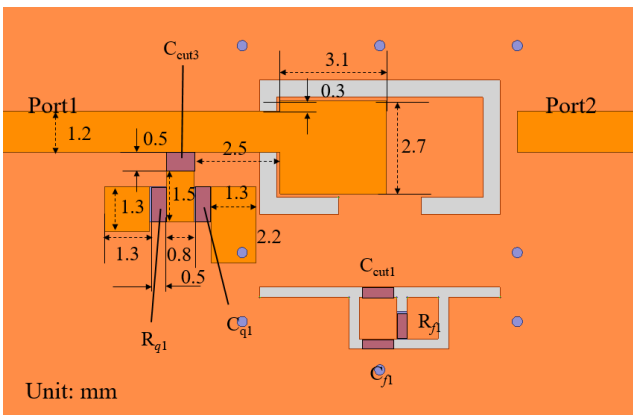

Fig. 14 Actual structure of the port.

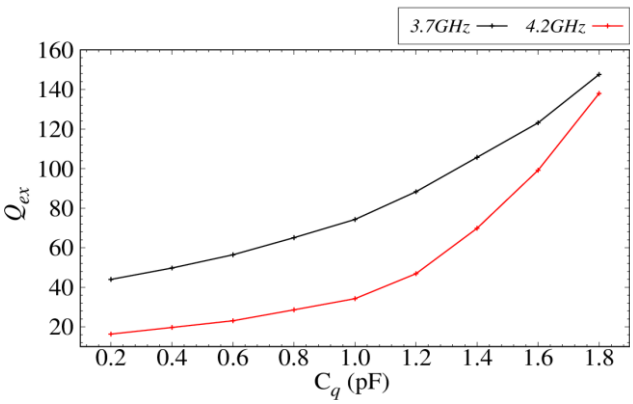

Fig. 15 At 3.7 GHz and 4.2 GHz, when changing C_q, the change tendency of Q_{ex}.

can be varied from 3.67 to 4.86 GHz. This circuit can satisfy the design requirements.

Compared with Fig. 4, we find that its variation range is smaller. It is considered that the original I-shaped slot has changed, and two small copper sheet structures and a series-connected DC blocking capacitor C_{cut1} (= 12 pF) have been added, which makes the equivalent capacitance value of the circuit smaller. However, the changing trend has stayed the same, and the method is still valid.

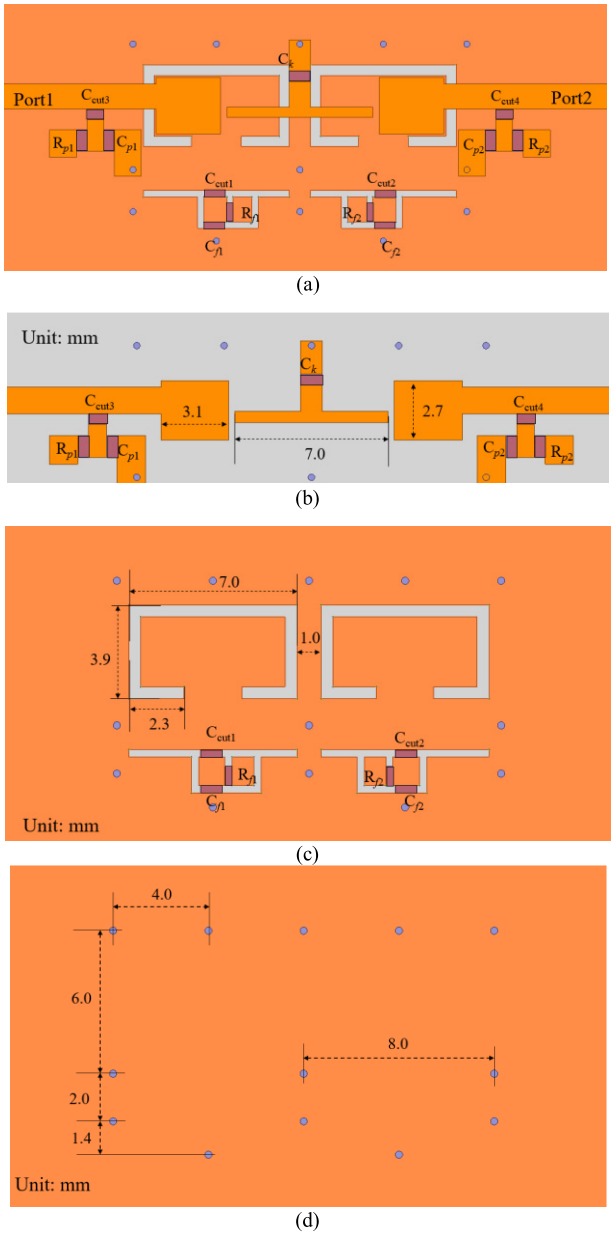

Fig. 16 (a) The overall structure of the tunable BPF. (b) Layer I. (c) Layer II. (d) Layer III.

3.3 Design of Bandwidth Adjustment Circuit

According to Fig. 9, the required capacitance and adjustment range of C_k is very small, and the varactor diode with the smallest capacitance that can be found is SMV-2201, with an adjustment range of 0.23–2.1pF. Then the f0 will be adjusted to 3.7GHz and 4.2GHz, respectively, and the coupling coefficients at different values of C_k are calculated.

The measurement circuit of the adjusted T-type non-resonator is shown in Fig. 12.

The value of k obtained from the circuit shown in Fig. 12 is collated in Fig. 13.

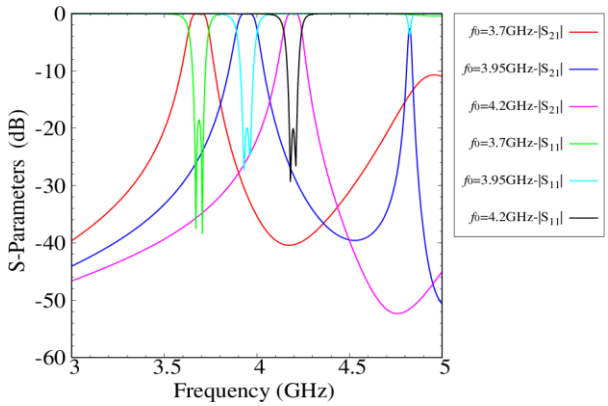

Fig. 17 Lossless scattering parameters at 3.7 GHz, 3.95 GHz, 4.2 GHz.

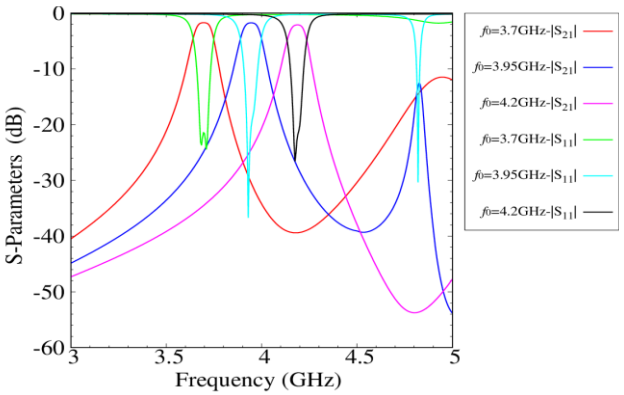

Fig. 18 Lossy scattering parameters at 3.7 GHz, 3.95 GHz, 4.2 GHz.

According to Fig. 13, when the value of C_k changes in the range of 0.2 pF–2 pF at 3.7 GHz, k changes from 0.0126 to 0.0192, reaching the target value 0.0191, and at 4.2 GHz, k changes from 0.0149 to 0.0265, reaching the target value 0.0169. The design requirements are met.

3.4 Design of the Adjustment Circuit of Q_{ex}

Regarding the adjustment of the Q_{ex}, the method in [27] is adopted, and its structure is shown in Fig. 14. Among them, C_q is the varactor diode of SMV-2201 (range: 0.23–2.1pF), C_{cut3} is the chip capacitor of 6 pF, and R_q is the chip resistor of 100 kΩ.

By simulating Fig. 14, the Q_{ex} under different capacitances of C_q can be obtained, and the simulation results are arranged in Fig. 15. According to Fig. 15, the Q_{ex} changes from 44 to 147.6 at 3.7 GHz when the capacitance of C_q changes from 0.2 pF to 1.8 pF, reaching the target value of 52.2. At 4.2 GHz, the Q_{ex} changes from 16.4 to 138, reaching the target value of 59.3. The design requirements are met.

3.5 Simulation of Tunable BPF

According to Sects. 3.2, 3.3, and 3.4 a tunable BPF can be composed, as shown in Fig. 16.

The circuit simulation in Fig. 16 can be obtained in Fig. 17 and Fig. 18.

According to the simulation results, the circuit can be adjusted from 3.7 to 4.2GHz, and the bandwidth can be controlled individually by controlling C_q and keeping the bandwidth at 100MHz. in the lossy case, the IL is 1.6 dB for f_0 = 3.7GHz. f_0 = 3.95GHz, the IL is 1.61 dB. f_0 = 4.2 GHz, the IL is 1.9 dB, to the maximum insertion loss.

According to Fig. 17 and Fig. 18, it is known that the circuit can meet the design requirements in Table 1. In addition, to more clearly demonstrate the effectiveness of the individual bandwidth regulation proposed in Sect. 2.2 of this paper, the simulation results for different bandwidths at 4.2 GHz are shown in Fig. 19. The bandwidths of 125 MHz, 150 MHz, and 175MHz are achieved respectively. The bandwidth tuning is mainly done by C_k, when the bandwidth is 125 MHz, C_k = 1.1 pF, C_f = 0.37 pF, and C_q = 0.95 pF. When the bandwidth is 150 MHz, C_k = 1.42 pF, C_f = 0.37 pF, and C_q = 0.87 pF. When the bandwidth is 175MHz, C_k = 2.2 pF, C_f = 0.39 pF, and C_q = 0.81 pF.

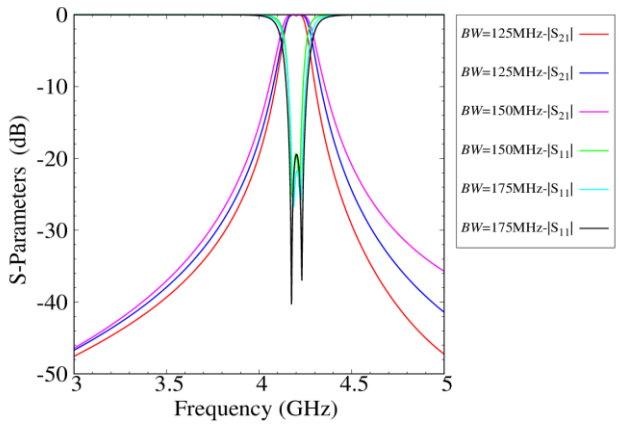

Fig. 19 Lossless scattering parameters with different bandwidths at 4.2 GHz.

4. Measured Results of Tunable BPF

The tunable BPF circuit in Fig. 16 was worked out in practice. The actual circuit structure is shown in Fig. 20.

In Fig. 20, the substrate uses MEGTRON7 R-5785(N) with a thickness of 0.5 mm, a relative dielectric constant of 3.4, and a dielectric dissipation factor of 0.002. The circuit size is $32 \times 18 mm^2$. C_f, C_k, and C_q all use MSV2201-040LF, R_f and R_q all use 667-ERJ-PA2F1003X, C_{cut1} and C_{cut2} use UMK-105-CH060DW, C_{cut3} and C_{cut4} use UMK-105-CH120JW, and the input of the black wire is the DC voltage V_f that controls C_f, the input of the blue wire is the DC voltage V_k that controls C_k, and the yellow wire is the DC voltage V_q that controls C_q.

Figure 21 and Fig. 22 show the measurement results at different frequencies when the BW is held constant. When V_f = 6.6 V, V_k = 7.6 V, V_q = 23.5 V, f_0 = 4.65 GHz,

Table 2 Comparison of this work with other tunable BPFs.

Items	Type	f_0 (GHz)	Order	BW tuning	BW tuning range	Size ($\lambda_g \times \lambda_g$)	IL (dB)
[30]	DGS	2.87-3.63	2	no	-	0.19 × 0.25	3.6-2.4
[31]	HMSIW	2.5-3.2	1	no	-	0.22 × 0.18	3-1
[32]	Microstrip line	1.27-1.6	2	yes	67-107MHz@1.62GHz	0.16 × 0.11	3.35-1.6
[33]	SIW	1.24-1.8	3	yes	75-187MHz@1.5GHz	0.83 × 0.30	4-2.8
[17]	SIDGS	1.75-2.7	2	no	-	0.07 × 0.08	2.7-1.75
This work: simulation	SIDGS	3.7-4.2	2	yes	100-175@4.2GHz	0.33 × 0.18	1.9-1.6
measurement	SIDGS	4.65-4.85	2	yes	202-276@4.8GHz	-	4-10.3

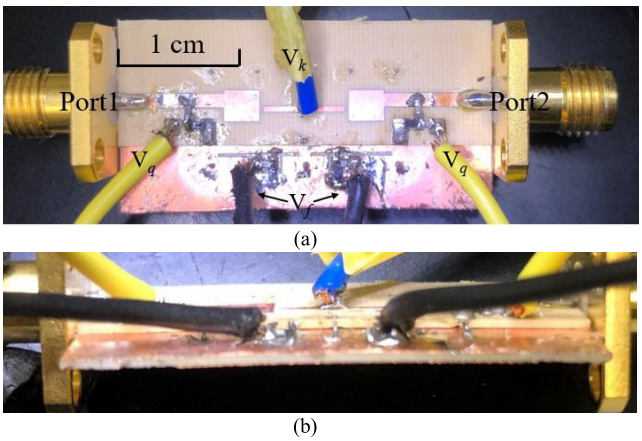

(a)

(b)

Fig. 20 The actual circuit structure of tunable SIDGS BPF. (a) top view. (b) front view.

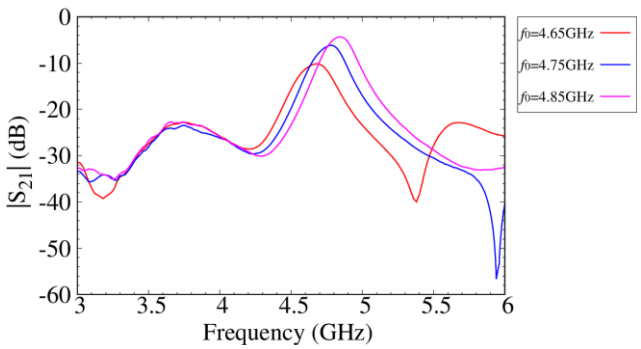

Fig. 21 The S_{21} at different center frequencies.

BW = 198 HMz, IL = 10.3 dB. When V_f = 8.2 V, V_k = 14.3 V, V_q = 23.5 V, f_0 = 4.75 GHz, BW = 201 HMz, IL = 6.8 dB. When V_f = 17.6 V, V_k = 18 V, V_q = 21.3 V, f_0 = 4.85 GHz, BW = 200 HMz, IL = 4 dB. All voltage values are readings from the constant voltage source. Comparing Fig. 18 and Fig. 21, it can be found that the measured results show a higher frequency, wider BW, larger IL, and tilted waveforms than the simulated results. The reasons are as follows: 1. During soldering, each component is not entirely asymmetrical, and there is an inevitable error in each component itself, which causes the frequency of the two resonators to be different, thus widening the BW and tilting the waveform. 2. Due to the larger BW, the required Q_{ex} becomes smaller, and a gap of about 0.1mm between the two substrates, which makes Q_{ex} larger, even if V_q is adjusted to 23.5 V (near the maximum voltage that the

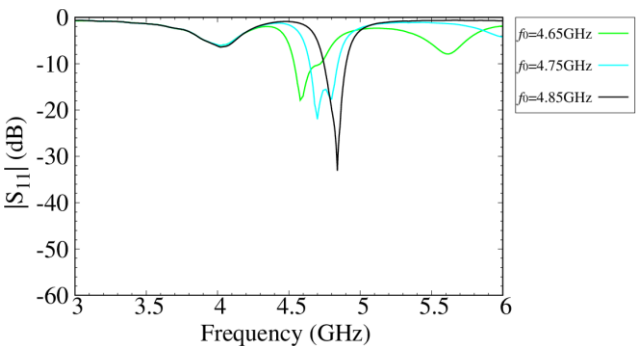

Fig. 22 The S_{11} at different center frequencies.

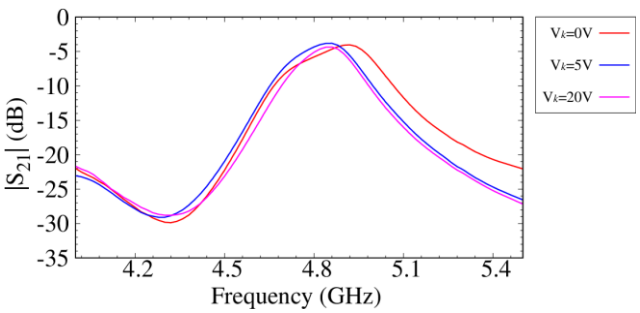

Fig. 23 The S_{21} for different bandwidths.

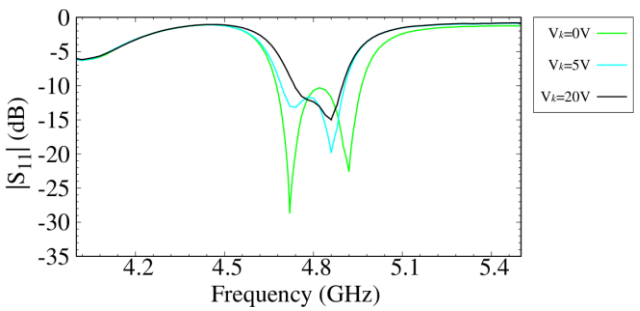

Fig. 24 The S_{11} for different bandwidths.

SMV2201 can withstand after voltage division). It cannot be reduced to the target value, causing IL to increase sharply. 3. The ideal components are used in the simulation, but the influence of parasitic inductance and parasitic capacitance of various components at high frequencies, in reality, will become apparent, which results in higher insertion loss and a higher resonant frequency.

Figure 23 and Fig. 24 show the measurement results

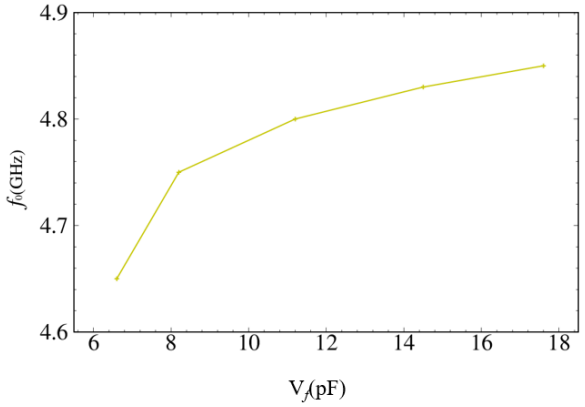

Fig. 25 The relationship between V_f and f_0.

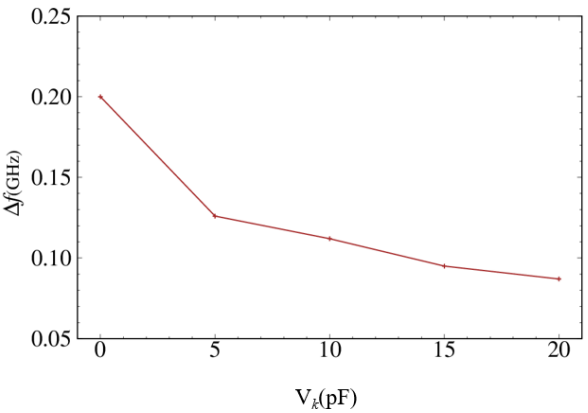

Fig. 26 The relationship between V_k and Δf.

under different bandwidths when f_0 is 4.8 GHz. When V_k changes from 20 V to 0 V, BW changes from 202 MHz to 276 MHz. Figure 23 also has the same problem as Fig. 21. However, through Fig. 21, Fig. 22, Fig. 23 and Fig. 24, it can be demonstrated the amount of their variation decreases as the voltage increases that the adjustable method proposed in this paper is effective and can achieve independent control of frequency and bandwidth. If the manufacturing process is improved, a circuit close to the simulation result can be obtained. About the improvement methods: 1. In the case of conditions permitting, we can use such as low temperature co-fired ceramic substrate to make the circuit to reduce the structural error. 2. Use higher precision chip capacitors, resistors, and varactor diodes to reduce the degree of inconsistency in the center frequency of the resonator.

To further demonstrate the controllability of f_0 and BW, the relationship between V_f and f_0, and the relationship between V_k and Δf are shown in Fig. 25 and Fig. 26, respectively. Δf represents the bandwidth between the two resonant frequencies. f_0 becomes higher as V_f increases, and Δf decreases as V_k increases, but the amount of variation decreases as the voltage increases. Due to insufficient external Q, the IL will increase as the frequency becomes lower, resulting in the waveform becoming indistinguishable, and its maximum tuning range cannot be known. However, it can be determined that the maximum tuning range of f_0 contains 4.65–4.85 GHz, and the maximum tuning range of Δf contains 0.87–0.2 GHz, and the maximum insertion loss at 4.65 GHz is 10.3 dB.

Finally, a comparison with other tunable miniaturization BPFs is made in Table 2. The tunable center frequency and bandwidth are achieved while maintaining the miniaturization.

5. Conclusion

This paper proposes a new independently adjustable method of frequency and bandwidth based on SIDGS BPF and proves the method's effectiveness through simulation and actual measurement.

Acknowledgments

This work is partly supported by the VLSI Design and Education Center (VDEC) at the University of Tokyo in collaboration with Keysight Technologies Japan, Ltd.

References

[1] D. Tang and X. Luo, "Compact Filtering Balun With Wide Stopband and Low Radiation Loss Using Hybrid Microstrip and Substrate-Integrated Defected Ground Structure," IEEE Microw. Compon. Lett., vol.31, no.6, pp.549–552, June 2021.
[2] R.A.R.Q.Y. Putri, S.F. Nuijihan, Y. Rafsyam, H. Mistialustina, H. Nusantara, and A. Munir, "Performance Analysis of Waveguide BPF Configured by SRR-Based Frequency Selective Surface and Its Equivalent Circuit," 2020 27th International Conference on Telecommunications (ICT), pp.1–4, 2020.
[3] K. Gong, W. Hong, H. Tang, and J. Chen, "C-band bandpass filter based on half mode substrate integrated waveguide (HMSIW) cavities," 2009 Asia Pacific Microwave Conference, pp.2591–2594, 2009.
[4] Y. Zhou, D. Tang, Y. Rao, Y. Dong, and X. Luo, "Miniaturized Tri-Band Bandpass Filter with Wide Stopband Using Stacked-Coupled SIDGS Resonators," 2022 IEEE/MTT-S International Microwave Symposium - IMS 2022, pp.468–471, 2022.
[5] D. Tang, C. Han, Z. Deng, H.J. Qian, and X. Luo, "Compact Bandpass Filter with Wide Stopband and Low Radiation Loss Using Substrate Integrated Defected Ground Structure," 2020 IEEE/MTT-S International Microwave Symposium (IMS), pp.671–674, 2020.
[6] C.-H. Lee, C.-I.G. Hsu, and H.-K. Jhuang, "Design of a New Tri-Band Microstrip BPF Using Combined Quarter-Wavelength SIRs," IEEE Microw. Compon. Lett., vol.16, no.11, pp.594–596, Nov. 2006.
[7] D. Tang, C. Han, Z. Deng, H.J. Qian, and X. Luo, "Substrate-Integrated Defected Ground Structure for Single- and Dual-Band Bandpass Filters With Wide Stopband and Low Radiation Loss," IEEE Trans. Microw. Theory Techn., vol.69, no.1, pp.659–670, Jan. 2021.
[8] Q. Li, H. Tang, D. Tang, Z. Deng, and X. Luo, "Compact SIDGS Filtering Power Divider With Three-Port 10-GHz Reflectionless Range," IEEE Trans. Circuits Syst. II, Exp. Briefs, vol.69, no.7, pp.3129–3133, July 2022.
[9] Y. Rao, J. Zhou, H.J. Qian, and X. Luo, "Compact Cross-Coupled Bandpass Filter with Wide Stopband and Low Radiation Loss Using SIDGS," 2021 IEEE Trans. Microw. Theory Techn.-S International Microwave Filter Workshop (IMFW), pp.30–32, 2021.
[10] N. Kumar and Y.K. Singh, "Compact Constant Bandwidth Tunable Wideband BPF With Second Harmonic Suppression," IEEE Microw.

Compon. Lett., vol.26, no.11, pp.870–872, Nov. 2016.
[11] N. Kumar, A.A. Gupta, V.K. Velidi, A. Subramanyam, V.S. Kumar, N. Ramalakshmi, D.V. Ramana, S. Narayana, and Y.K. Singh, "Constant Absolute Bandwidth Tunable BPF with Reconfigurable Bandwidth Using Stubs-Loaded Grounded MMR," 2021 IEEE Trans. Microw. Theory Techn.-S International Microwave and RF Conference (IMARC), pp.1–4, Dec. 2021.
[12] B. Lan, J. Xu, C. Guo, and J. Ding, "A Fully Tunable Bandpass Filter Using A Varactor-Tuned Short-Stub Loaded Resonator," 2018 International Conference on Microwave and Millimeter Wave Technology (ICMMT), pp.1–3, May 2018.
[13] B. Pradhan and B. Gupta, "Novel tunable band reject filter using RF MEMS technology," Proceedings of the 2014 IEEE Students' Technology Symposium, pp.335–340, March 2014.
[14] S.S. Saberhosseini, B.A. Ganji, and A. Ghorbani, "Tunable and dual-band HMSIW resonator using RF MEMS capacitor," 2017 Iranian Conference on Electrical Engineering (ICEE), pp.279–282, May 2017.
[15] N.K. Tiwari, P.K. Varshney, S.P. Singh, and M.J. Akhtar, "Shape Perturbed Tunable Planar RF Resonator for the Dielectric Measurement in wide frequency range," 2019 8th Asia-Pacific Conference on Antennas and Propagation (APCAP), pp.666–667, Aug. 2019.
[16] D. Jiang, Y. Liu, X. Li, G. Wang, and Z. Zheng, "Tunable Microwave Bandpass Filters With Complementary Split Ring Resonator and Liquid Crystal Materials," IEEE Access, vol.7, pp.126265–126272, 2019.
[17] D. Tang, H.J. Qian, Y. Dong, and X. Luo, "Compact 1.75–2.7 GHz Tunable BPF With Wide Stopband Up to 9.5 GHz Using Harmonic-Controlled SIDGS Resonators," IEEE Trans. Circuits Syst. II, Exp. Briefs, vol.69, no.11, pp.4228–4232, Nov. 2022.
[18] A.Z. El Dein, A.B. Abdel-Rahman, R.E. Fat-Helbary, and A.M. Montaser, "Tunable - compact bandstop defected ground structure (DGS) with lumped element," 2010 7th International Multi-Conference on Systems, Signals and Devices, pp.1–3. 2010.
[19] N.K. Tiwari, Y. Tiwari, P. Azad, and M.J. Akhtar, "Novel design for CSRR based electronically steered compact S-band microwave resonator," 2017 IEEE Asia Pacific Microwave Conference (APMC), pp.1238–1241, Nov. 2017.
[20] A. Boutejdar, A. Ibrahim, M. Challal, A.A. Wael, and E. Burte, "Extracting of compact tunable BPF from LPF using single T-DGS-resonator and 0.25PF/0.5PF Chip Monolithic Ceramic Capacitors," 2015 4th International Conference on Electrical Engineering (ICEE), pp.1–5, Dec. 2015.
[21] J. Vehmas and S. Tretyakov, "Omega transmission lines," 2013 7th International Congress on Advanced Electromagnetic Materials in Microwaves and Optics, pp.10–12, Sept. 2013.
[22] C. Sabah, F. Urbani, and S. Uckun, "High-pass filter characteristic of Bloch impedance in a left-handed transmission line," 2007 19th International Conference on Applied Electromagnetics and Communications, pp.1–4, Sept. 2007.
[23] M. Gil, J. Bonache, J. Selga, J. Garcia-Garcia, and F. Martin, "Broadband Resonant-Type Metamaterial Transmission Lines," IEEE Microw. Compon. Lett., vol.17, no.2, pp.97–99, Feb. 2007.
[24] C. Han, D. Tang, Z. Deng, H.J. Qian, and X. Luo, "Filtering Power Divider With Ultrawide Stopband and Wideband Low Radiation Loss Using Substrate Integrated Defected Ground Structure," IEEE Microw. Compon. Lett., vol.31, no.2, pp.113–116, Feb. 2021.
[25] J.-S. Hong, Microstrip Filters for RF/Microwave Applications, 2 ed., Wiley, pp.6–18, 2011.
[26] K. Nishikawa and M. Muraguchi, "Dual-Mode Frequency Tunable Planar Filter Design with Capacitive Coupling Technique," 2018 IEEE International Symposium on Radio-Frequency Integration Technology (RFIT), pp.1–3, 2018.
[27] C.-F. Chen, "Design of a Microstrip Three-State Switchable and Fully Tunable Bandpass Filter With an Extra-Wide Frequency Tuning Range," IEEE Access, vol.8, pp.66438–66447, 2020.
[28] J.-S. Hong, Microstrip Filters for RF/Microwave Applications, 2 ed., Wiley, p.215, 2011.
[29] J.-S. Hong, Microstrip Filters for RF/Microwave Applications, 2 ed., Wiley, p.40, 2011.
[30] A. Boutejdar, A. Omar, M. Senst, E.P. Burte, A. Batmanov, and R. Mikuta, "A new design of a tunable WLAN-band pass filter using a combination of varactor device, RF-choke and Hairpin-defected ground structure," 2011 6th European Microwave Integrated Circuit Conference, pp.506–509, Oct. 2011.
[31] D.E. Senior, X. Cheng, and Y.-K. Yoon, "Electrically Tunable Evanescent Mode Half-Mode Substrate-Integrated-Waveguide Resonators," IEEE Microw. Compon. Lett., vol.22, no.3, pp.123–125, March 2012.
[32] N. Kumar, S. Narayana, and Y.K. Singh, "Constant Absolute Bandwidth Tunable Symmetric and Asymmetric Bandpass Responses Based on Reconfigurable Transmission Zeros and Bandwidth," IEEE Trans. Circuits Syst. II, Exp. Briefs, vol.69, no.3, pp.1014–1018, March 2022.
[33] M. Deng and D. Psychogiou, "Tune-All Substrate-Integrated-Waveguide (SIW) Bandpass Filters," 2019 49th European Microwave Conference (EuMC), pp.876–879, Oct. 2019.

Weiyu Zhou received his B.S. in electrical engineering from Southwest Petroleum University, Chengdu, China, in 2016, and received his M.S. in 2020 at the Graduate School of Informatics and Engineering from the University of Electro-Communications in Tokyo, Japan. He is now studying toward his doctorate at the Graduate School of the University of Electro-Communications.

Koji Wada received his doctorate in engineering from Yamaguchi University, Yamaguchi, Japan, in 1999. From 1999 to 2004, he was a research associate with the Department of Electrical Engineering and Electronics at Aoyama Gakuin University in Kanagawa, Japan. From 2004 to 2015, he worked as an associate professor at the Department of Electronic Engineering at the University of Electro-Communications in Tokyo, Japan. He is currently a Professor in the Graduate School of Informatics and Engineering at the University of Electro-Communications. His research interests include resonators, filters, multiplexers, multiband circuits, tunable circuits, periodic structure and metamaterial circuits. Dr. Wada is a member of the Institute of Electronics, Information and Communication Engineers (IEICE) and the Institute of Electrical Engineers of Japan (IEEJ).